

# Impact of voltage and frequency on electrical characteristics of MIS capacitors with triphenylamine layer



Selcuk Izmirli <sup>a</sup>, Sukru Cavdar <sup>b</sup>, Pınar Oruc <sup>b</sup>, Serkan Eymur <sup>c</sup>, Nihat Tuğluoğlu <sup>c,\*</sup>

<sup>a</sup> Department of Advanced Technologies, Gazi University, 06500, Ankara, Turkiye

<sup>b</sup> Department of Physics, Faculty of Science, Gazi University, Ankara, Turkiye

<sup>c</sup> Department of Energy Systems Engineering, Faculty of Engineering, Giresun University, Giresun, Turkiye

## ARTICLE INFO

### Keywords:

TPA  
MIS-Type capacitor  
Active interface trap density  
Series resistance

## ABSTRACT

This study examines the effect of triphenylamine (TPA) interlayers on the electrical properties of Al/TPA/p-Si metal-interlayer/insulator material-semiconductor (MIS) capacitors. Using Gaussian software, TPA molecular structure was optimized, and HOMO-LUMO energy levels were simulated. Capacitance-conductance-voltage (*C-G-V*) measurements were performed at room temperature over  $-4\text{ V}$  to  $+4\text{ V}$  and  $50\text{ kHz}$ – $700\text{ kHz}$ . AFM and SEM analysis showed TPA films were smooth with a uniform thickness of about 178 nm. The *C-V* characteristics revealed a frequency-dependent decrease in capacitance, indicating a continuous distribution of interface states. Barrier height ( $\Phi_B$ ) increased from 0.305 eV at 50 kHz to 0.655 eV at 700 kHz, while the active interface trap density ( $D_{it}$ ) decreased from  $6.73 \times 10^{12} \text{ eV}^{-1} \text{ cm}^{-2}$  to  $3.23 \times 10^{11} \text{ eV}^{-1} \text{ cm}^{-2}$ . Additionally, the accumulating region exhibited low series resistance values (between 6.88 and 8.44  $\Omega$ ). These results suggest that TPA thin films are effective for MIS capacitors.

## 1. Introduction

Organic devices, including resistors, capacitors, Schottky diodes, photodiodes, and thin-film transistors, have been extensively studied, and significant advancements have been made in their manufacturing technologies [1–4]. Since 2000, researchers have increasingly utilized organic materials to develop high-efficiency devices with optimal electrical properties [5–10]. They have enhanced the metal/semiconductor (MS) contact by modifying the barrier height and improving the quality of MS structure through the replacement of  $\text{SiO}_2$ , typically used in MS connections, with organic or inorganic interfacial layers. An alternative method to design rectifying devices involves creating metal-interlayer/insulator-semiconductor (MIS) structures. In MIS diodes, rectification is achieved by the pinning of the Fermi level by interface states. It is simple to modify the interface structure of MIS diodes by adding suitable inorganic metal oxides [11–14], polymers [15–17], or functional organic molecules [18–22]. The voltage range over which MIS diodes are utilized typically varies depending on the application type, the semiconductor technology employed, and the thickness of the oxide layer. Generally, MOS diodes are operational across various voltage ranges. Specifically, in the low voltage range (1.2 V–3.3 V), MOS diodes are commonly used in modern integrated circuits

(ICs), particularly within low-voltage digital CMOS circuits [23–25].

In a recent study, Sunkur et al. investigated the electrical and charge transport characteristics of the Al/1PA2N/p-Si MIS device using current-voltage techniques [26]. They determined the barrier height, series resistance, and interface state density of the MIS structure. In another work, these researchers fabricated an Al/ERY/p-Si MIS structure and calculated its electrical characteristics using capacitance-voltage and current-voltage measurements [27]. Pakma et al. also created an MIS-type structure with a Coronene interlayer and subsequently determined the electrical characteristics of this structure [19]. Additionally, Imer et al. fabricated a Sn/C<sub>14</sub>H<sub>15</sub>N<sub>3</sub>/p-Si heterojunction using the spin coating technique and measured its electrical characteristics through current-voltage and capacitance-voltage measurements [28].

Triphenylamine (TPA) is an organic compound that is highly effective for surface coating in Schottky device designs [29]. TPA is also widely used as a donor group in the literature due to its excellent electron-donating properties [30–33]. It features continuous conjugation between the central nitrogen atom and three neighboring phenyl groups, making it an ideal organic structure for donor- $\pi$ -acceptor (D- $\pi$ -A) systems in recent years [34–37]. Structures containing triphenylamine molecules generally reduce the gap between the highest occupied molecular orbital (HOMO) and the lowest unoccupied

\* Corresponding author. Giresun University Faculty of Engineering Campus of Güre, 28200, Giresun, Turkiye.

E-mail address: [nihat.tugluoglu@giresun.edu.tr](mailto:nihat.tugluoglu@giresun.edu.tr) (N. Tuğluoğlu).

molecular orbital (LUMO), resulting in absorption in the near-infrared region [38,39].

Cavdar et al. presented an Al/TPA/p-Si/Al diode structure and they examined the experimental *I-V* characteristics at various illumination intensities to explore its electrical and photo response properties [40]. In this study, we focus on the detailed frequency-dependent electrical characterization of TPA MIS capacitors, emphasizing the role of the insulator-semiconductor interface, particularly interface states and series resistance, on the device parameters. Consequently, the capacitance-voltage and conductance-voltage characteristics of the TPA organic layered Al/TPA/p-Si/Al structure were studied under dark conditions at room temperature across a frequency range of 50 kHz–700 kHz and a voltage range of  $\pm 4$  V to investigate the impacts of interface state density and series resistance on the electrical characteristics of the structure.

In this study, the active interface trap density ( $D_{it}$ ) values of the TPA MIS capacitor were calculated using the Hill-Coleman method and found to decrease with increasing frequency, while the barrier height ( $\phi_B$ ) values increased. Voltage-dependent profiles of  $D_{it}$  and series resistance ( $R_s$ ) were determined through capacitance measurements in the low-high frequency range ( $C_{LF} - C_{HF}$ ) using the Nicollian-Brews method. Furthermore, based on the obtained results, we evaluated the potential applications of TPA as an interfacial layer in MIS-based technology. To our knowledge, no prior research has been conducted on the capacitors in TPA thin films. Additionally, this study examined frequency-dependent electrical parameters, including barrier height ( $\phi_B$ ), Fermi level ( $E_F$ ), depletion region width ( $W_D$ ), and acceptor atom concentration ( $N_A$ ). These findings provide new insights into the electrical behavior of TPA MIS structures and their potential for future electronic applications.

## 2. Experimental section

In this study, we utilized a p-type Si semiconductor with (100) surface orientation,  $1 \Omega\cdot\text{cm}$  resistivity,  $525 \mu\text{m}$  thickness, and a polished surface. The Si semiconductor was chemically cleaned to eliminate organic and inorganic contaminants. It was ultrasonically cleaned with chloroform, methanol, and acetone for 5 min each. Subsequently, it was washed with HF for 1 min and rinsed thoroughly with ultrapure water to remove the oxide layer. Immediately after cleaning, a  $\sim 1500 \text{ \AA}$  thick layer of high-purity (99.999 %) Al was thermally evaporated onto the back matte surface of the p-Si substrate at a pressure of  $10^{-6}$  Torr using a physical evaporation system. The p-Si/Al structure was annealed at  $575^\circ\text{C}$  for 5 min in a dry nitrogen atmosphere to achieve a low-resistance ohmic contact.

For the organic layer formation, 0.4 g of TPA ( $(\text{C}_5\text{H}_4\text{NCH}_2)_3\text{N}$ ) was dissolved in 10 ml of chloroform and stirred for 10 min. A TPA organic thin film was then deposited on the polished surface of the p-Si substrate using the spin coating method, first at 500 rpm for 10 s and then at 3000 rpm for 20 s. Rectifying contacts were created on the organic layer using

a mask and the thermal evaporation method (radius of the contact was 1.10 mm). SEM images of the diode and the AFM measurements were taken using a HITACHI SU5000 Field Emission Scanning Electron Microscope (FE-SEM) and with a NanoMagnetics hpAFM device, respectively. Capacitance and conductance measurements were performed using a Keithley 4230 source meter. A diagram of the Al/p-Si MIS-type capacitor fabrication process with a TPA interlayer is shown in Fig. 1.

## 3. Results and discussion

We performed calculations using density functional theory (DFT) at the B3LYP/6-31G (d,p) level to determine the electronic properties of TPA (see Fig. 2). This analysis includes the determination of the HOMO and LUMO energy levels, as well as their distribution and location, which are crucial for understanding the molecular features. DFT-calculated energy levels of the LUMO and HOMO for the TPA compound are illustrated in Fig. 3. The values of TPA's HOMO and LUMO energies, along with other molecular characteristics computed from these values, are presented in Table 1 (see Fig. 4).

When two semiconductors with differing electron affinities, band gaps ( $E_g$ ), and work functions are combined to form a heterojunction diode, energy band discontinuities occur due to the alignment of the Fermi level. When the free interfacial states align with the vacuum level,

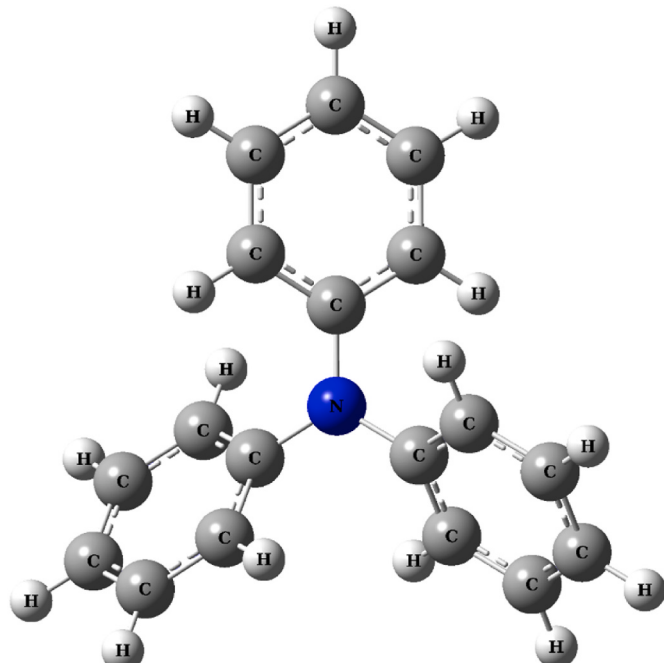


Fig. 2. The optimized molecular structure of TPA compound.

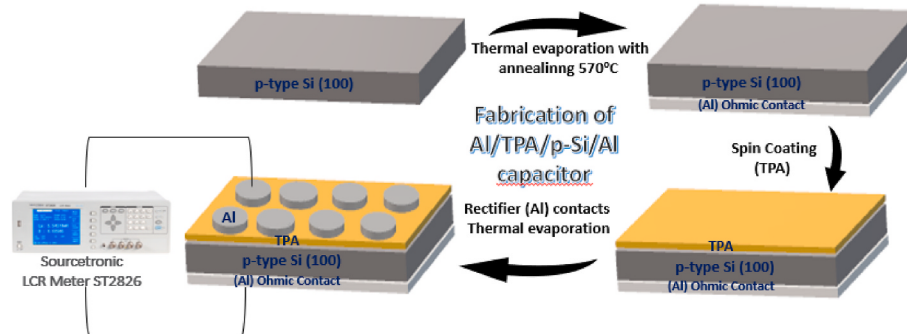
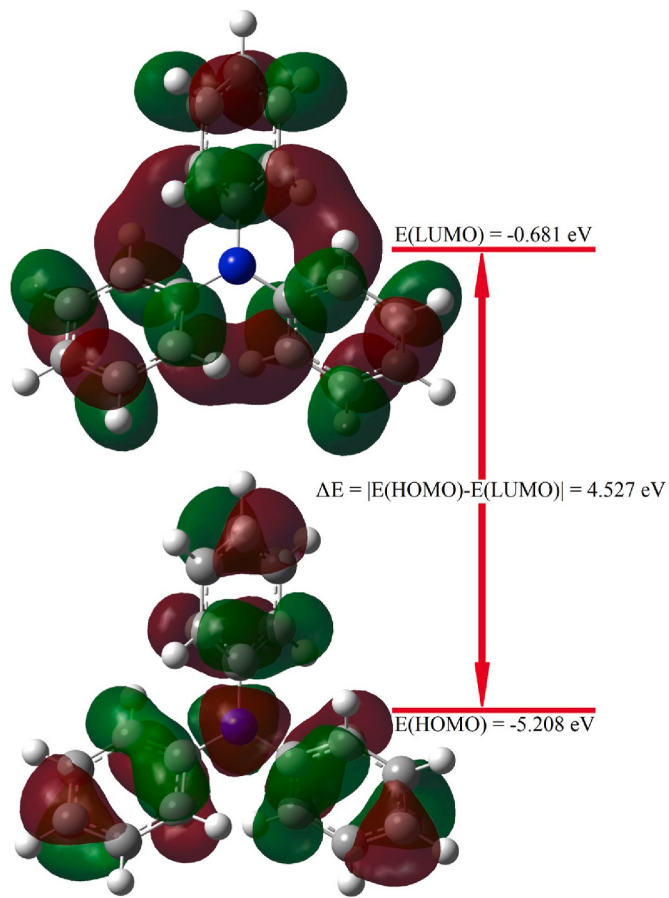
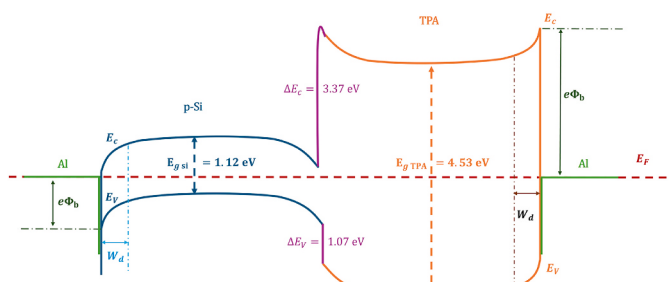


Fig. 1. Schematic diagram of Al/TPA/p-Si/Al MIS-type capacitor fabrication procedure.



**Fig. 3.** DFT calculated energy levels of LUMO and HOMO of TPA compound.



**Fig. 4.** The energy band diagram of Al/TPA/p-Si/Al MIS-type capacitor.

**Table 1**  
Molecular descriptors derived from the HOMO and LUMO energy levels of TPA.

Parameters (eV)	Value (eV)
E <sub>LUMO</sub> (eV)	-0.681
E <sub>HOMO</sub> (eV)	-5208
Energy bandgap  E <sub>HOMO</sub> - E <sub>LUMO</sub>	4527
Ionization potential ( $I = -E_{HOMO}$ )	5208
Electron affinity ( $A = -E_{LUMO}$ )	0,681
Chemical hardness ( $h = (I-A)/2$ )	2263
Chemical softness ( $z = 1/h$ )	0,221
Electronegativity ( $\chi = (I+A)/2$ )	2945
Chemical potential ( $\mu = -(I+A)/2$ )	-2945
Electrophilicity index ( $w = \mu^2/2h$ )	1915
Maximum charge transfer index ( $\Delta N_{max.} = -\mu/h$ )	1301

the discontinuities in the conduction band are equal to the difference in the electron affinities of the semiconductors ( $\Delta E_c = \chi_{Si} - \chi_{TPA}$ ), according to Anderson's affinity rule. Furthermore, the valence band discontinuities ( $\Delta E_v$ ) are calculated as  $\Delta E_v = \Delta E_g - \Delta E_c$ , where  $\Delta E_g$  represents the difference in the band gaps between the two semiconductors.

**Fig. 5a** shows the SEM image and **Fig. 5b** shows the schematic diagram of the TPA diode. The SEM images in **Fig. 5a** shows that the TPA organic layer has an average thickness of 170 nm.

**Fig. 6(a)** and (b) and (c) show two- and three-dimensional (2D and 3D) AFM images of the TPA organic thin film  $1 \times 1 \mu m^2$ ,  $3 \times 3 \mu m^2$ , and  $5 \times 5 \mu m^2$  scales. The root mean square (rms) surface roughness of the TPA films were found as 14.46 nm, 17.81 nm, and 24.76 nm, respectively. The surface morphology of the TPA film were reasonably smooth, with uniform grain distribution. The values of the roughness parameters have confirmed the validity and significance of establishing a uniform interfacial contact between the TPA and the rectifier contact, which enhances the performance of electronic devices [41].

The electrical properties of the Al/TPA/p-Si/Al capacitor were investigated under forward and reverse bias voltages at various frequencies. **Fig. 7** presents the capacitance-voltage ( $C_m - V$ ) characteristics of the MIS structure measured at  $\pm 4$  V across a frequency range of 50 kHz–700 kHz. The  $C-V$  curve exhibited accumulation, depletion, and inversion regions, with capacitance variations observed as a function of voltage and frequency [42]. Notably, prominent peaks were observed in the  $-1$  V–0 V range. The magnitude of these peaks decreased and shifted towards lower voltages with increasing frequency. This behavior is attributed to the reconfiguration of interface states [43].

There was a rapid decrease in  $C_m$  value from  $-1$  V to  $+1$  V within the  $\pm 1$  V voltage range. This region corresponded to the depletion region, where charge carriers are depleted [44]. At positive voltage values (greater than  $+1$  V), there was no significant change in capacitance regardless of frequency, as the defect charges do not have sufficient time to respond to the applied voltage. This region is known as the inversion region, characterized by a change in the polarity of the charge carriers [45]. When a certain positive voltage threshold is exceeded, minority carriers accumulate in the inversion layer compared to majority carriers. Although the voltage increases, the depletion zone reaches its maximum depth [46].

**Fig. 8** illustrates the measured conductance-voltage ( $G_m - V$ ) characteristics of the Al/TPA/p-Si/Al MIS-type capacitor at increasing frequencies. It was observed that conductance increases with frequency, which was an expected outcome since the frequency-dependent behavior of conductance is the inverse of that of capacitance [47,48]. This variation in conductance confirms the presence of interfacial states. Additionally, conductance decreased with increasing voltage at all frequencies, and in the positive voltage region, all conductance values converge.

**Fig. 9** represents the capacitance-frequency ( $C_m - f$ ) characteristics measured at negative bias voltage, highlighting the diode's accumulation and depletion regions. The measurements reveal that the capacitance value decreased with increasing frequency across all voltages. Specifically, at  $-1$  V, the capacitance values were 18.1 nF at 50 kHz and 4.28 nF at 700 kHz. This reduction in capacitance at higher frequencies may be attributed to the inability of majority of carriers to follow the AC signal [49]. The capacitance at high frequencies is primarily due to space charge capacitance [50]. Furthermore, the variation in capacitance in such heterojunction structures can be ascribed to the relaxation time and the series resistance effects arising from the interface states [51].

**Fig. 10** shows the measured conductance-frequency ( $G_m - f$ ) characteristics of the Al/TPA/p-Si/Al MIS-type capacitor under negative voltage conditions. The data indicate that the conductance of the capacitor increased with rising frequency across all voltage levels. This observation was consistent with the anticipated behavior that the capacitance and conductance of a capacitor were inversely related to

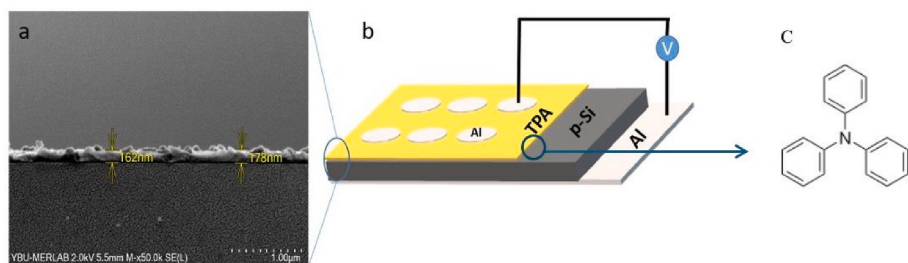


**Fig. 5.** (a) SEM image of TPA/p-Si structure, (b) Schematic diagram of Al/TPA/p-Si/Al capacitor.

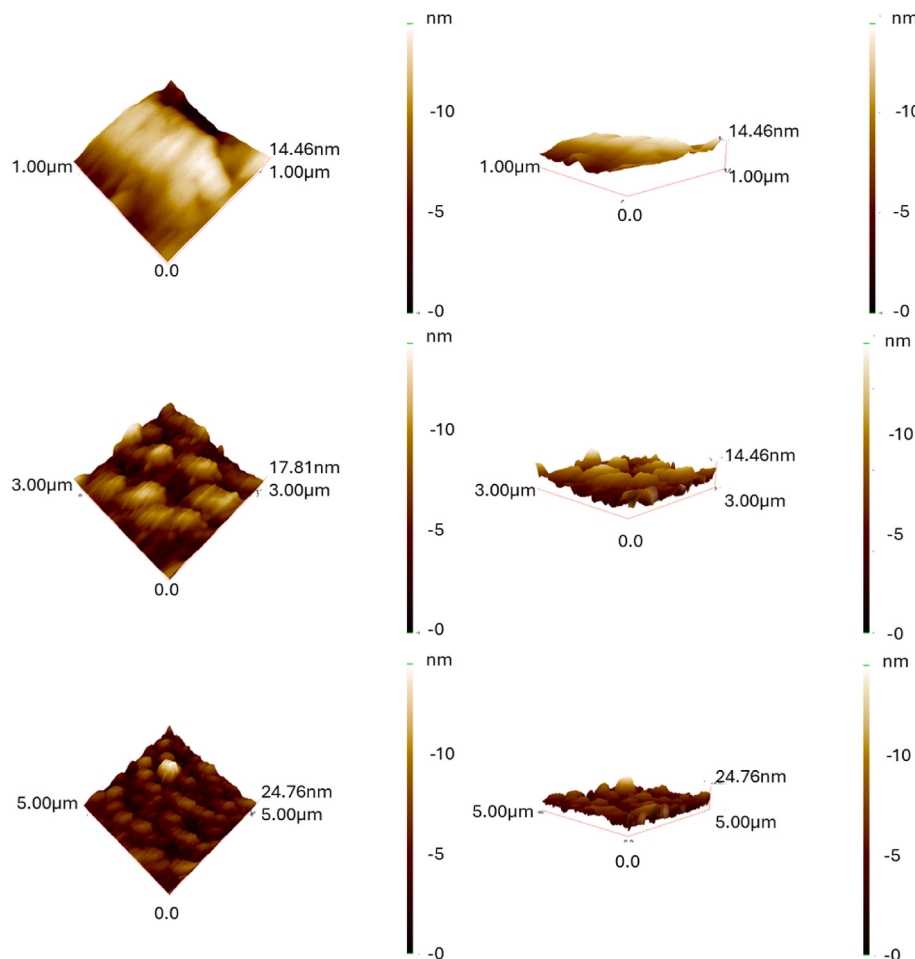


**Fig. 6.** (a)  $1 \times 1 \mu\text{m}^2$ , (b)  $3 \times 3 \mu\text{m}^2$ , (c)  $5 \times 5 \mu\text{m}^2$  AFM images (2D and 3D) of TPA/p-Si structures.

increasing frequency [52]. The observed increased in conductance with frequency can be attributed to the interface states, the relaxation time of the charges, as well as the dynamics of carriers trapped between empty and occupied states at the Fermi level [53].

Series resistance ( $R_s$ ) is a critical parameter that can induce non-ideal behavior in capacitors. It can be derived from both capacitance and conductance values using the expression proposed by Nicollian and Goetzberger [54,55]:

$$R_s = \frac{G_m}{G_m^2 + (\omega C_m)^2} \quad (1)$$

Here,  $C_m$  and  $G_m$  represent the measured capacitance and conductance, respectively, and  $\omega$  denotes the angular frequency. Fig. 11 illustrates the  $R_s - V$  curves at various frequencies, demonstrating that  $R_s$  decreased with increasing frequency. It was evidence that the series resistance

varies with both voltage and frequency under positive bias. Notably, the series resistance value decreased with increasing frequency under negative bias. This behavior of  $R_s$  can be attributed to the distribution of localized interface states [56].

The frequency-dependent  $R_s$  values of the TPA/p-Si structure is given for different voltages in Fig. 12. It is observed that the series resistance decreases with an increase in frequency, ranging from 50 kHz to 700 kHz, irrespective of the applied voltage. Although the series resistance values exhibited similar behavior across the spectrum, they were significantly higher under positive bias compared to negative bias. The series resistance values in the accumulation region ( $R_s$ ) were determined to be  $8.44 \Omega$  at 50 kHz and  $6.88 \Omega$  at 700 kHz. The  $R_s$  values at various frequencies are presented in Table 2.

To eliminate the series resistance effect that adversely affects the capacitance and conductivity measurements of the diode, corrected

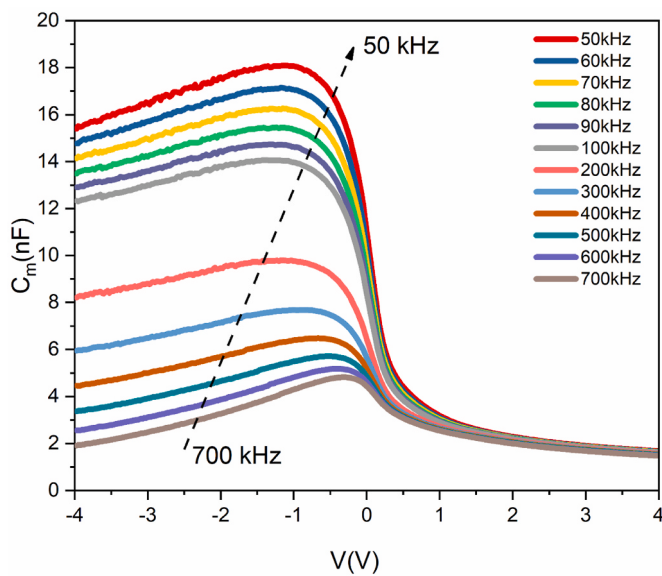


Fig. 7. Measured capacitance–voltage plots of the Al/TPA/p-Si Schottky diode.

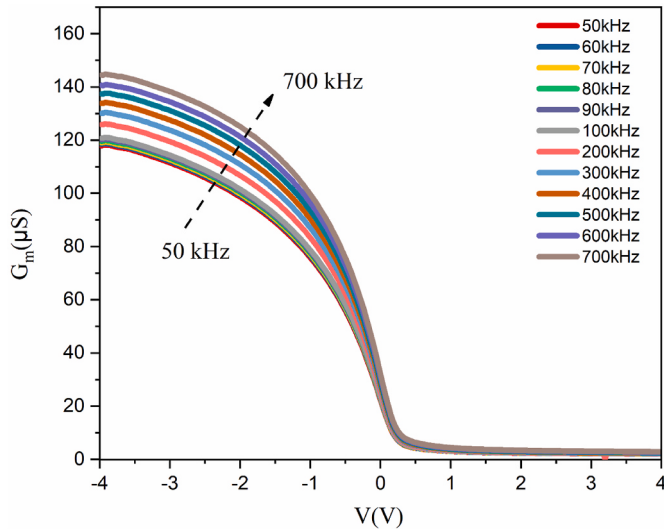


Fig. 8. Measured conductance–voltage plots of the Al/TPA/p-Si/Al MIS-type capacitor at different frequencies.

capacitance ( $C_c$ ) and conductance ( $G_c$ ) values can be obtained by using the following Eqs. (2) and (3) [55]:

$$C_c = \frac{(G_m^2 + \omega^2 C_m^2) C_m}{a^2 + \omega^2 C_m^2}, \quad G_c = \frac{(G_m^2 + \omega^2 C_m^2) a}{a^2 + \omega^2 C_m^2} \quad (2)$$

$$a = G_m - (G_m^2 + \omega^2 C_m^2) R_s \quad (3)$$

where  $C_m$  and  $G_m$  are the measured capacitance and conductance, respectively.

Figs. 13 and 14 show the voltage-dependent corrected capacitance ( $C_c$ ) and corrected conductance ( $G_c/\omega$ ) graphs of the Al/TPA/p-Si/Al MIS-type capacitor at various frequencies, respectively, calculated using Eqs. (2) and (3). As depicted in Fig. 13, the capacitance values decreased with increasing frequency. Across all frequencies, the corrected capacitance reached its maximum value in the voltage range of -3.5V to -4V.

Fig. 14 shows that the corrected conductance of the capacitor also decreased with increasing frequency. The conductance values attained

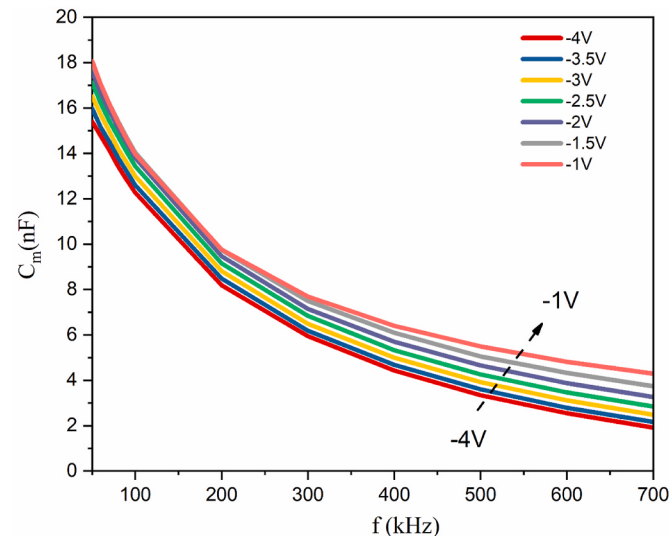


Fig. 9. Measured capacitance–frequency plots of the Al/TPA/p-Si/Al MIS-type capacitor at different voltages.

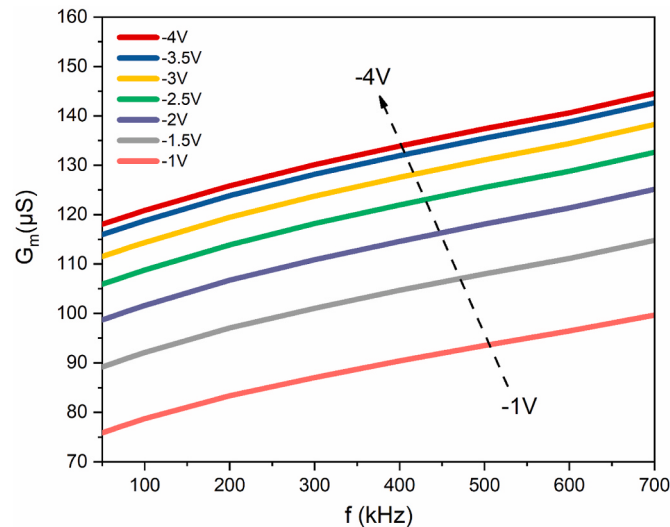
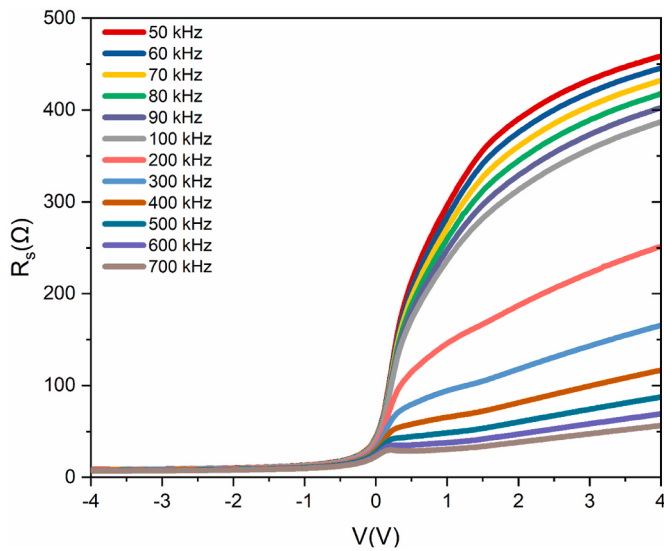


Fig. 10. Conductance–frequency plots of the Al/TPA/p-Si/Al MIS-type capacitor at different voltages.

their maximum between -2.5V and -3.5V at all frequencies, and as the frequency increased, these peaks shifted towards lower negative voltages. This behavior clearly confirms the existence of an interface states [54,57]. The voltage range where the maximum peak values in the  $G_c/\omega$  graph (Fig. 14) were observed corresponds to the depletion region of the  $C_c$ - $V$  graph shown in Fig. 13. This phenomenon is illustrated in Fig. 15.

The  $C_c$ – $V$  and  $G_c/\omega$  plots of the fabricated capacitor at 700 kHz are shown in Fig. 15. The region where the rectified conductance of the diode peaks corresponded to the depletion region of the rectified capacitance, and this peak indicated the active interface trap density ( $D_{it}$ ) [58]. The most common method used to calculate active interface trap density ( $D_{it}$ ) is the equation derived by Hill-Coleman [59]. Using the depletion region in the corrected capacitance graph for each frequency and the data at the maximum points of the corrected conductance curve corresponding to this region, the values of the interfacial state density of the produced capacitor can be calculated with the following Eq. (4) [60].



**Fig. 11.** Series resistance-voltage plots of the Al/TPA/p-Si/Al MIS-type capacitor at different frequency.

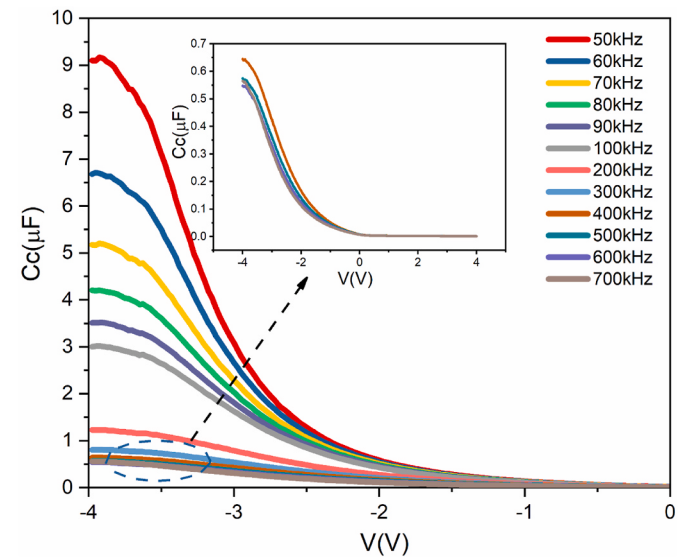


**Fig. 13.** Corrected capacitance-voltage plots of the Al/TPA/p-Si/Al MIS-type capacitor.

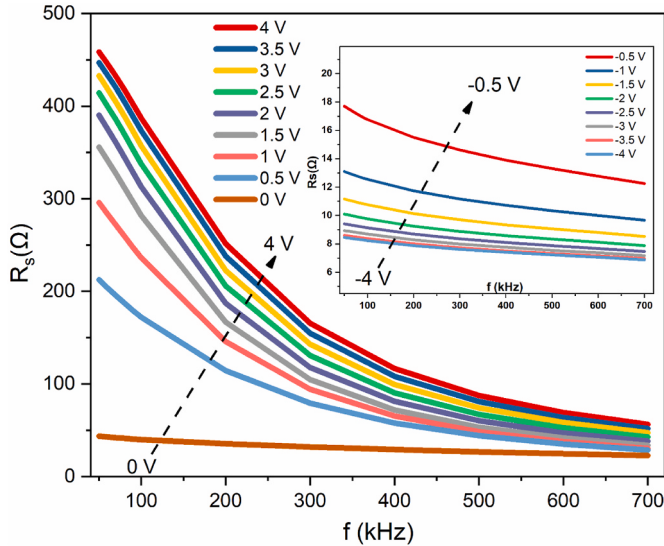


**Fig. 12.** Series resistance-frequency plots of the Al/TPA/p-Si Schottky diode at different voltages.

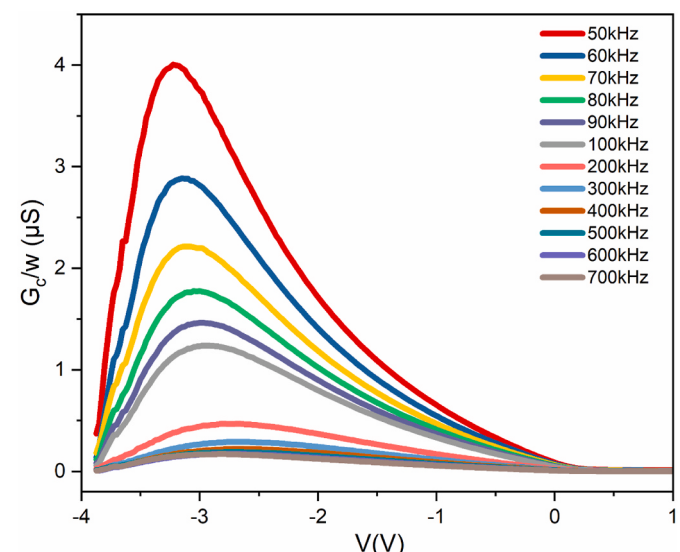


**Fig. 14.** Corrected conductance-voltage plots of the Al/TPA/p-Si/Al MIS-type capacitor.

**Table 2**

Electrical parameters of Al/TPA/p-Si/Al MIS-type capacitor determined from capacitive and conductive properties in the frequency range of 50 kHz–700 kHz.

f (kHz)	$V_{peak}$ (V)	$C_c$ ( $\mu\text{F}$ )	$G_c/\omega$ ( $\mu\text{S}$ )	$R_s$ ( $\Omega$ )	$D_{it} \times 10^{11}$ ( $\text{eV}^{-1}\text{cm}^{-2}$ )
50	-3.23	4.580	4.006	8.44	67.36
60	-3.15	3.389	2.887	8.40	49.81
70	-3.13	2.733	2.216	8.35	40.43
80	-3	2.032	1.777	8.31	30.43
90	-2.98	1.753	1.466	8.27	25.53
100	-2.98	1.579	1.240	8.23	23.20
200	-2.78	0.642	0.469	7.87	9.30
300	-2.63	0.389	0.292	7.61	5.43
400	-2.68	0.323	0.221	7.40	4.47
500	-2.7	0.285	0.189	7.21	3.87
600	-2.78	0.270	0.172	7.06	3.59
700	-2.8	0.256	0.170	6.88	3.23

$$D_{it} = \frac{2 \left( \frac{G_{c,max}}{\omega} \right)}{qA} \left[ \left( \frac{G_{c,max}}{\omega C_i} \right)^2 + \left( 1 - \frac{C_c}{C_i} \right)^2 \right]^{-1} \quad (4)$$

Here,  $C_i$  is the capacitance of the interface layer in the accumulation region and is calculated from the maximum value of the  $C_c$  curve.  $A$  is the area of the capacitor,  $G_{c,max}$  is the maximum of the rectified  $G_c/\omega - V$  curve, and  $C_c$  is the capacitance of the diodes corresponding to  $G_{c,max}$ . Using the voltage-dependent parameters given in Figs. 13 and 14 in Eq. (4), the active interface trap density of the capacitor at different frequencies was calculated and presented in Table 2 and shown in Fig. 16. Analyses of the results revealed that the obtained value was consistent with the findings in the literature [54,61].

As seen in Fig. 16 and in Table 2,  $D_{it}$  of the Al/TPA/p-Si/Al MIS-type capacitor decreased with increasing frequency.  $D_{it}$  decreased slowed down in high frequency regions. The obtained  $D_{it}$  values are  $6.73 \times 10^{12}$  and  $3.23 \times 10^{11} \text{ eV}^{-1} \text{cm}^{-2}$  for 50 kHz and 700 kHz, respectively. The values obtained for  $D_{it}$  are similar to the values reported for the

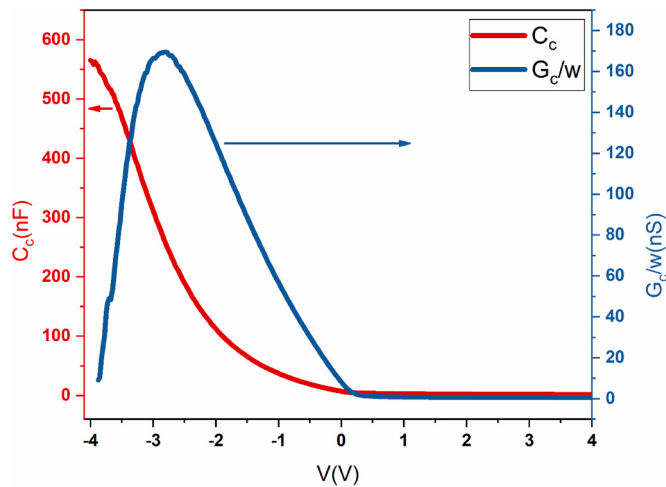


**Fig. 15.** Corrected capacitance and conductance-voltage curves of the capacitor at 700 kHz.

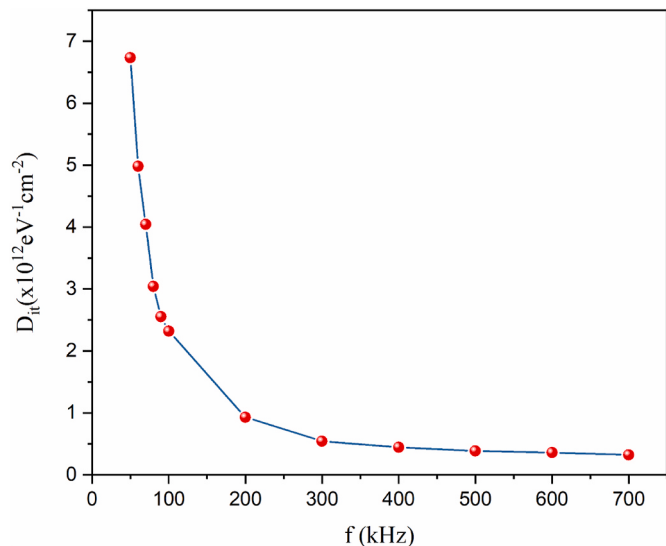


**Fig. 16.** The variation plot of  $D_{it}$  with frequency in Al/TPA/p-Si/Al MIS-type capacitor.

fabricated MIS-type structures in the literature [44,54,62–64]. Furthermore, the series resistance of a device is affected by the localized interface states in a frequency-dependent manner. At low frequencies, these states can increase the resistance by trapping charge carriers. As the frequency increases, the resistance generally decreases as the trapped states become less influential due to the rapid switching of the signal. A negative bias typically reduces the impact of these interface states on series resistance by modifying their energy levels or reducing their interaction with the carriers. This interplay is crucial in designing high-frequency electronic devices and optimizing their performance by managing interface states and understanding their impact on resistance.

Depending on the voltage, the low-high frequency capacitance approach can also be used to calculate the active interface trap density ( $D_{it}$ ). The fabricated capacitor was subjected to this approach, and the active interface trap densities were computed using the following equation [65–67]:

$$D_{it} = \frac{1}{qA} \left[ \left( \frac{1}{C_{LF}} - \frac{1}{C_i} \right)^{-1} - \left( \frac{1}{C_{HF}} - \frac{1}{C_i} \right)^{-1} \right] \quad (5)$$

**Fig. 17** shows the variation of  $D_{it} - V$ , which was obtained from the

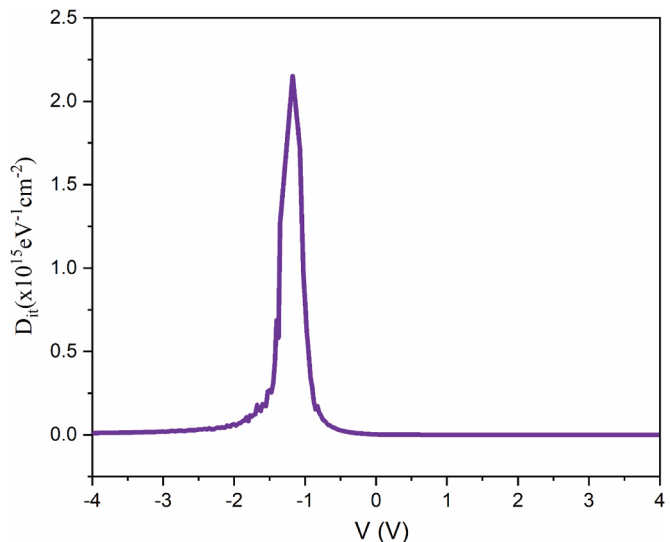


**Fig. 17.** The variation plot of  $D_{it}$  with voltage in Al/TPA/p-Si/Al MIS-type capacitor.

$C_{LF} - C_{HF}$  approach using low frequency (50 kHz) and high frequency (700 kHz). **Fig. 17** illustrates the continuous distribution of  $D_{it}$ , which remains constant between  $-4$  V and  $-2$  V, exhibits a peak at  $-1.18$  V, subsequently decreases to  $0$  V, and eventually stabilizes at  $+4$  V. The peak value of the  $N_{ss}$  is observed at approximately  $-1.18$  V. This corresponds to a magnitude on the order of  $10^{15}$  eV, a sufficiently high value to stabilize the Fermi level at the surface of the Si substrate [68].

**Fig. 18** shows the inverse-bias  $C_c^{-2} - V$  plots obtained from the  $C_c - V$  plots of the Al/TPA/p-Si/Al MIS-type capacitor from 50 kHz to 700 kHz and in the dark. Based on the linearity of the  $C_c^{-2} - V$  plot of the Al/TPA/p-Si/Al MIS-type capacitor, it is possible to estimate the trap densities.

The relation between capacitance and applied voltage for diodes is given by [62].

$$C^{-2} = \frac{2(V_{bi} + V)}{q\epsilon_s \epsilon_0 A^2 N_A} \quad (6)$$

where  $A$ ,  $C$ ,  $q$ ,  $\epsilon_s$ ,  $\epsilon_0$  are the diode area, the depletion region capacitance, the electron charge, the semiconductor permeability ( $\epsilon_s = 11.8$  for Si),

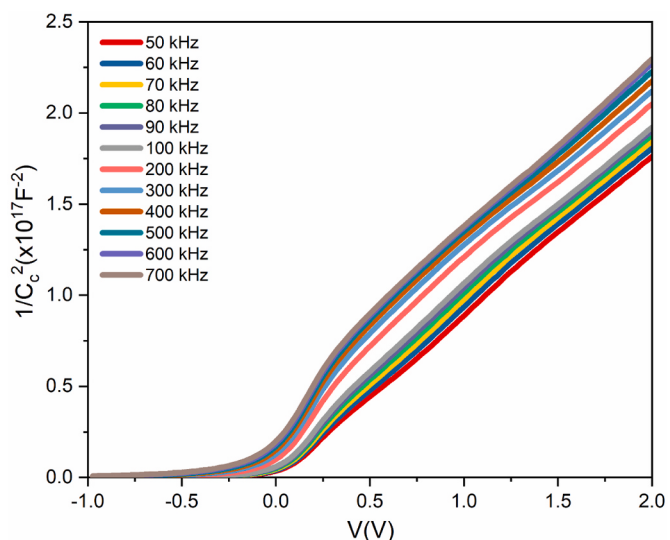


**Fig. 18.**  $C_c^{-2}-V$  plots for Al/TPA/p-Si Schottky diode.

and the vacuum permeability ( $\epsilon_0 = 8.85 \times 10^{-12} \text{ F/m}$ ), respectively. The  $V_{bi}$  values were extracted from Eq. (6) by examining the linear relation between  $C_c^{-2}$  and V in the strong bias region in Fig. 18.  $V_{bi}$  is the diffusion potential at zero bias, which is determined from the extrapolation of the linear  $C_c^{-2} - V$  plot to the V-axis were found to be in the range of 0.162–0.508 V for the frequency variations from 50 kHz to 700 kHz.  $N_A$  is acceptor concentration which is given as [54]

$$N_A = N_V \exp\left(\frac{qV_p}{kT}\right) \quad (7)$$

Where  $N_V$  is the density of states in the valence band for p-Si,  $V_p$  is the potential difference between the Fermi energy level ( $E_F$ ) and the peak of the valence band of Si and is equal to  $E_F$ . This value can be calculated after obtaining the  $N_A$  carrier concentration via Eq. (7). The value of  $V_p$  is obtained from the following relation [42,54].

$$V_p = E_F = kT \ln\left(\frac{N_y}{N_A}\right) \quad (8)$$

The barrier height ( $\Phi_B$ ) of the diodes can be obtained using the following relation [55].

$$\Phi_B(C - V) = V_{bi} + V_p \quad (9)$$

By using the  $C_c^{-2} - V$  measurement, the barrier height and acceptor carrier concentration values for the Al/TPA/p-Si devices were extracted as 0.655 eV and  $3.567 \times 10^{16} \text{ cm}^{-3}$  from linear region of its  $C_c^{-2} - V$  characteristic for 700 kHz, respectively.

In addition, the depletion layer width ( $W_D$ ) was determined from  $C_c^{-2} - V$  plots by the following Eq. (10) [37,60].

$$W_D = \sqrt{\frac{2\epsilon_S \epsilon_0 V_{bi}}{qN_A}} \quad (10)$$

Various electrical parameters of the Al/TPA/p-Si diode such as is the diffusion potential ( $V_{bi}$ ), doping concentration of acceptor atoms ( $N_A$ ), Fermi energy level ( $E_F$ ), depletion width ( $W_D$ ) barrier height ( $\Phi_B$ ) were calculated from  $C_c^{-2} - V$  plots and listed in Table 3 for different frequencies.

In Table 3, there have been an increase in the  $V_{bi}$ ,  $E_F$  and  $\Phi_B$  values depending on the increasing frequency.  $N_A$  and  $W_D$  values also increase with increasing frequency. As can be seen from the table, the interface states and series resistance of the diode affect its important electrical properties depending on the frequency.

#### 4. Conclusions

This work examined a metal-interlayer/insulator-semiconductor (MIS) capacitor made of Al/TPA/p-Si. The spin coating technique was used to create an interlayer of TPA organic compound. The TPA molecule was examined using SEM and AFM techniques. The surface examination carried out using the AFM technique reveals that the surface morphology of the spin-coated TPA film layer is smooth, with uniform grain distribution. The forward and reverse bias capacitance-voltage ( $C - V$ ) and conductance-voltage ( $G - V$ ) characteristics of the Al/TPA/p-Si MIS-type capacitor were measured in the frequency range of 50 kHz–700 kHz and  $\pm 4$  V at room temperature. The observed capacitance and conductance were also adjusted to yield the actual MIS capacitance without the influence of series resistance. To examine the interface states distribution of the capacitor, the corrected conductance-voltage ( $G - V$ ) and capacitance-voltage ( $C - V$ ) characteristics at various frequencies were also computed. Following the required series resistance modifications, notable alterations in the capacitance have been noticed, particularly on the conductance curves. Furthermore, corrected  $C_c^{-2} - V$  plots were used to determine the device's key parameters, including the barrier height ( $\Phi_B$ ), depletion width ( $W_D$ ), Fermi energy level ( $E_F$ ), acceptor doping concentration ( $N_A$ ), and diffusion

**Table 3**

Values of different parameter parameters calculated from  $C_c^{-2} - V$  plots of the Al/TPA/p-Si/Al MIS-type capacitor.

f (kHz)	$V_{bi}$ (V)	$N_A \times 10^{16}$ (cm $^{-3}$ )	$E_F$ (eV)	$W_D \times 10^{-8}$ (cm)	$\Phi_B$ (eV)
50	0.162	4.122	0.143	2367	0.305
60	0.197	4.084	0.143	1939	0.341
70	0.226	4.048	0.144	1697	0.369
80	0.249	4.021	0.144	1538	0.393
90	0.267	4.002	0.144	1432	0.411
100	0.284	3.991	0.144	1346	0.428
200	0.390	3.916	0.144	982	0.534
300	0.425	3.842	0.145	900	0.570
400	0.447	3.777	0.145	856	0.593
500	0.470	3.686	0.146	815	0.616
600	0.483	3.626	0.146	793	0.629
700	0.508	3.567	0.147	753	0.655

potential ( $V_{bi}$ ), as a function of frequency.

Electrical parameters of the capacitor at 700 kHz; the active interface trap density ( $D_{it}$ ), series resistance ( $R_s$ ),  $V_{bi}$ ,  $N_A$ ,  $E_F$ ,  $W_D$ , and  $\Phi_B$  are 3.23  $\times 10^{11} \text{ eV}^{-1} \text{ cm}^{-2}$ , 6.885  $\Omega$ , 0.508 V,  $3.567 \times 10^{16} \text{ cm}^{-3}$ , 0.147 eV,  $0.753 \times 10^{-3} \mu\text{m}$ , 0.655 eV, respectively. When the Al/TPA/p-Si diode is compared with the literature, the  $R_s$  value of the diode is low, and the  $D_{it}$  value is like that of MOS diodes with organic interfaces. The active interface trap density of the diode is of the order of  $10^{12} \text{ eV}^{-1} \text{ cm}^{-2}$ , which is suitable for electronic device technology, indicating that it can also be used in electronic applications. In other words, the TPA organic compound can be used as an interfacial layer in MIS-based applications with the computed active interface trap density and barrier height.

#### Data availability

The datasets generated during and/or analyzed during the current study are available from the Corresponding author upon reasonable request.

#### Ethical approval

The authors maintain high standards of personal conduct, practicing honesty in all our professional relationships and endeavors.

#### CRediT authorship contribution statement

**Selcuk Izmirli:** Writing – original draft, Visualization, Investigation, Formal analysis. **Sukru Cavdar:** Writing – review & editing, Writing – original draft, Visualization, Supervision, Resources, Project administration, Investigation. **Pinar Oruc:** Writing – original draft, Investigation, Formal analysis. **Serkan Eymur:** Writing – original draft, Visualization, Resources. **Nihat Tuğluoğlu:** Writing – review & editing, Writing – original draft, Visualization, Investigation.

#### Declaration of competing interest

The authors declare that they have no known competing financial interests or personal relationships that could have appeared to influence the work reported in this paper.

#### Acknowledgments

This work was supported financially by the Gazi University Research Fund (BAP) (Grant Numbers: FDK-2022-7701 and FOA-2022-7389).

#### References

- [1] H.H. Gullu, D.E. Yıldız, S.O. Hacıoglu, A. Cirpan, L. Toppare, Phys. Scripta 98 (2023) 015819.
- [2] S. Yadav, P. Mittal, S. Negi, Phys. Scripta 99 (2024) 025940.

- [3] S. Demirezen, A. Dere, H.G. Çetinkaya, A.G. Al-Sehem, A.A. Al-Ghamdi, F. Yakuphanoglu, *Phys. Scripta* 98 (2023) 115916.
- [4] T. Kim, C. Lee, W. Lee, H. Kim, Y. Kim, *ACS Appl. Electron. Mater.* 4 (2022) 130.
- [5] M.F. Şahin, E. Taşçı, M. Emrullahoglu, H. Gökc, N. Tuğluoğlu, S. Eymur, *Physica B* 614 (2021) 413029.
- [6] Ş. Aydoğan, Ü. İncekara, A.R. Deniz, A. Türüt, *Solid State Commun.* 150 (2010) 1592.
- [7] Ş. Aydoğan, Ü. İncekara, A.R. Deniz, A. Türüt, *Microelectron. Eng.* 87 (2010) 2525.
- [8] I. Orak, M. Toprak, A. Turut, *Phys. Scripta* 89 (2014) 115810.
- [9] T. Ganj, S.M. Rozati, Y. Azizian-Kalandaragh, G. Pirgholi, *Givi Phys. Scr.* 98 (2023) 055803.
- [10] S. Cavdar, Y. Demiroglmez, N. Turan, H. Koralay, N. Tuğluoğlu, L. Arda, *ECS J. Solid State Sci. Technol.* 11 (2022) 025001.
- [11] A. Birkan Selçuk, N. Tuğluoğlu, S. Karadeniz, S. Bilge, *Ocak Physica B* 400 (2007) 149.
- [12] N. Tuğluoğlu, Ş. Altindal, A. Tataroğlu, S. Karadeniz, *Microelectron. J.* 35 (2004) 731.
- [13] F.D. Akgül, S. Eymur, Ü. Akin, Ö.F. Yüksel, H. Karadeniz, N. Tuğluoğlu, *J. Mater. Sci. Mater. Electron.* 32 (2021) 15857.
- [14] M.O. Erdal, A. Koçyigit, M. Yıldırım, *Microelectron. Reliab.* 106 (2020) 113591.
- [15] E.E. Tanrıku, S. Demirezen, Ş. Altindal, I. Uslu, *J. Mater. Sci. Mater. Electron.* 28 (2017) 8844.
- [16] S. Demirezen, A. Kaya, Ö. Vural, Ş. Altindal, *Mater. Sci. Semicond. Process.* 33 (2015) 140.
- [17] F. Yakuphanoglu, B.F. Şenkal, *J. Phys. Chem. C* 111 (2007) 1840.
- [18] N. Kaplan, E. Taşçı, M. Emrullahoglu, H. Gökc, N. Tugluoglu, S. Eymur, *J. Mater. Sci. Mater. Electron.* 32 (2021) 16738.
- [19] O. Pakma, S. Çavdar, H. Koralay, N. Tugluoglu, Ö. Yüksel *Physica B* 527 (2017) 1.
- [20] A.O. Tezcan, S. Eymur, E. Taşçı, M. Emrullahoglu, N. Tugluoglu, *J. Mater. Sci. Mater. Electron.* 32 (2021) 12513.
- [21] A. Ben Ahmed, M. Benhaliliba, Y.S. Ocak, A. Ayeshamariam, C.E. Benouis, *Opt. Mater.* 126 (2022) 112071.
- [22] M. Benhaliliba, A. Ben, Ahmed *Chemistry Africa* 7 (2024) 1629.
- [23] N. Arora, MOSFET DC model, in: N. Arora (Ed.), *MOSFET Models for VLSI Circuit Simulation: Theory and Practice*, Springer Vienna, Vienna, 1993, p. 230.
- [24] N. Arora, Dynamic model, in: N. Arora (Ed.), *MOSFET Models for VLSI Circuit Simulation: Theory and Practice*, Springer Vienna, Vienna, 1993, p. 325.
- [25] S.M. Sze, *Physics of Semiconductor Devices*, Wiley, New York, 1981.
- [26] M. Sunkur, O. Gullu, *J. Phys. Chem. Solid.* 178 (2023) 111360.
- [27] M. Sunkur, C. Aytug-Ava, O. Gullu, *Surface. Interfac.* 39 (2023) 102900.
- [28] A. Gencer Imer, A. Korkut, W.A. Farooq, A. Dere, M. Atif, A. Hanif, A. Karabulut, *J. Mater. Sci. Mater. Electron.* 30 (2019) 19239.
- [29] X. Lian, Z. Zhao, D. Cheng, *Mol. Cryst. Liq. Cryst.* 648 (2017) 223.
- [30] A. Hossein Habibi, P. Josse, P.S. Marqués, P. Blanchard, C. Cabanetos, *ChemPhotoChem* 6 (2022) e202200114.
- [31] V.D. Gupta, A.B. Tathe, V.S. Padalkar, P.G. Umape, N. Sekar, *Dyes Pigments* 97 (2013) 429.
- [32] T. Keawin, N. Prachumrak, S. Namuangruk, S. Pansay, N. Kungwan, S. Maensiri, S. Jungsuttiwong, T. Sudyoadsuk, V. Promarak, *RSC Adv.* 5 (2015) 73481.
- [33] Y. Yuan, G.-Q. Zhang, F. Lu, Q.-X. Tong, Q.-D. Yang, H.-W. Mo, T.-W. Ng, M.-F. Lo, Z.-Q. Guo, C. Wu, C.-S. Lee, *Chem. Asian J.* 8 (2013) 1253.
- [34] R. Rybakiewicz, M. Zagorska, A. Pron, *Chem. Pap.* 71 (2017) 243.
- [35] M. Erdogan, A.R. Deniz, Z. Çaldırın, *J. Photochem. Photobiol., A* 443 (2023) 114877. A.
- [36] D.H. Lee, M.J. Lee, H.M. Song, B.J. Song, K.D. Seo, M. Pastore, C. Anselmi, S. Fantacci, F. De Angelis, M.K. Nazeeruddin, M. Grätzel, H.K. Kim, *Dyes Pigments* 91 (2011) 192.
- [37] F. Bahrani, R. Hameed, S. Resan, M. Al-Anber, *Acta Phys. Pol.* 141 (2022) 561. A.
- [38] W.A. Arcos, R.R. Guimaraes, B. Insuasty, K. Araki, A. Ortiz, *J. Mol. Struct.* 1111 (2016) 157.
- [39] C.O. Sánchez, E. Schott, X. Zárate, D. MacLeod-Carey, P. Sobarzo, N. Gatica, *Polym. Bull.* 72 (2015) 897.
- [40] S. Çavdar, S. Izmirli, H. Koralay, N. Turan, S. Eymur, N. Tuğluoğlu, *ECS J. Solid State Sci. Technol.* 12 (2023) 045001.
- [41] A.M. Nawar, M. Abd-Elsalam, A.M. El-Mahalawy, M.M. El-Nahass, *Appl. Phys. A* 126 (2020) 113.
- [42] S. Duman, F.S. Ozcelik, B. Gurbulak, D. Korucu, O. Baris, G. Turgut, *Mater. Sci. Semicond. Process.* 28 (2014) 20.
- [43] M. Ulusoy, Ş. Altindal, P. Durmus, S. Özçelik, Y. Azizian, Kalandaragh *J. Mater. Sci.: Mater. Electron.* 32 (2021) 13693.
- [44] S. Çavdar, Y. Demiroglmez, N. Turan, H. Koralay, N. Tuğluoğlu, *J. Mater. Sci. Mater. Electron.* 33 (2022) 22932.
- [45] A. Dere, M. Soylu, F. Yakuphanoglu, *Mater. Sci. Semicond. Process.* 90 (2019) 129.
- [46] L. Dou, Y. Yang, J. You, Z. Hong, W.-H. Chang, G. Li, Y. Yang, *Nat. Commun.* 5 (2014) 5404.
- [47] A. Tataroğlu, A.A. Al-Ghamdi, F. El-Tantawy, W.A. Farooq, F. Yakuphanoglu, *Appl. Phys. A* 122 (2016) 220.
- [48] M.A. Manthrammel, I.S. Yahia, M. Shkir, S. AlFaify, H.Y. Zahran, V. Ganesh, F. Yakuphanoglu, *Solid State Sci.* 93 (2019) 7.
- [49] M. Sharma, S.K. Tripathi, *Mater. Sci. Semicond. Process.* 41 (2016) 155.
- [50] Ö. Güllü, Ş. Aydoğan, A. Türüt, *Semicond. Sci. Technol.* 23 (2008) 075005.
- [51] S. Duman, B. Gürbulak, S. Doğan, A. Türüt, *Vacuum* 85 (2011) 798.
- [52] M. İlhan, M.M. Koç, B. Coşkun, M. Erkovan, F. Yakuphanoglu, *J. Mater. Sci. Mater. Electron.* 32 (2021) 2346.
- [53] R. Lok, E. Budak, E. Yilmaz, *J. Mater. Sci. Mater. Electron.* 31 (2020) 3111.
- [54] N. Tuğluoğlu, Ö.F. Yüksel, S. Karadeniz, H. Şafak, *Mater. Sci. Semicond. Process.* 16 (2013) 786.
- [55] E.H. Nicollian, J.R. Brews, *MOS (Metal Oxide Semiconductor) Physics and Technology*, Wiley, 1982.
- [56] G.F. Salem, E.A.A. El-Shazly, A.A.M. Farag, I.S. Yahia, *Appl. Phys. A* 124 (2018) 744.
- [57] A.G. Al-Sehem, A. Tataroğlu, A. Karabulut, A. Dere, A.A. Al-Ghamdi, F. Yakuphanoglu, *JOM* 75 (2023) 3587.
- [58] N. Tugluoglu, *Nucl. Instrum. Methods Phys. Res., Sect. B* 254 (2007) 118.
- [59] W.A. Hill, C.C. Coleman, *Solid-State Electron.*, vol. 23, 1980, p. 987.
- [60] S.R. Forrest, P.H. Schmidt, *J. Appl. Phys.* 59 (1986) 513.
- [61] F. Parlaktürk, S. Altindal, A. Tataroglu, M. Parlak, A. Agasiev, *Microelectron. Eng.* 85 (2008) 81.
- [62] Ü. Akin, Ö.F. Yüksel, E. Taşçı, N. Tuğluoğlu, *Silicon* 12 (2020) 1399.
- [63] S. Demirezen, I. Orak, Y. Azizian-Kalandaragh, Ş. Altindal, *J. Mater. Sci. Mater. Electron.* 28 (2017) 12967.
- [64] M. Benhaliliba, Y.S. Ocak, *Appl. Phys. A* 130 (2024) 371.
- [65] G. Ersoz, Y. İ, Y. Azizian-Kalandaragh, O. İ, A. Ş, *IEEE Trans. Electron Devices* 63 (2016) 2948.
- [66] M. Soylu, I.S. Yahia, F. Yakuphanoglu, W.A. Farooq, *J. Appl. Phys.* 110 (2011).
- [67] Ç. Bilkan, S. Zeyrek, S.E. San, Ş. Altindal, *Mater. Sci. Semicond. Process.* 32 (2015) 137.
- [68] H. Uslu, I. Dökme, I.M. Afandiyeva, S. Altindal, *Surf. Interface Anal.* 42 (2010) 807.